Journal of Innovative Optical Health Sciences
Vol. 13, No. 2 (2020) 2050010 (11 pages)
© The Author(s)
DOI: 10.1142/S1793545820500108

Intraoperative imaging of oral-maxillofacial lesions using optical coherence tomography

Zihan Yang*, Jianwei Shang†, Chenlu Liu‡, Jun Zhang§,
Fang Hou* and Yanmei Liang*,¶
**Institute of Modern Optics, Nankai University*
Nankai, Tianjin 300350, P. R. China

†*Department of Oral Pathology, Tianjin Stomatological Hospital*
Hospital of Stomatology of Nankai University
Nankai, Tianjin 300041, P. R. China

‡*Department of Oral Medicine, Tianjin Stomatological Hospital*
Hospital of Stomatology of Nankai University
Nankai, Tianjin 300041, P. R. China

§*Department of Oral-Maxillofacial Surgery*
Tianjin Stomatological Hospital
Hospital of Stomatology of Nankai University
Nankai, Tianjin 300041, P. R. China
¶*ymliang@nankai.edu.cn*

Received 19 November 2019
Accepted 9 January 2020
Published 5 February 2020

Histopathological examination is still the gold standard for diagnoses of oral-maxillofacial lesions, but it is invasive and time-consuming. Optical coherence tomography (OCT) provides a kind of noninvasive, label-free, real-time and high-resolution imaging technology. In this study, in order to assess the feasibility of OCT in oral clinical application, fresh excised tissue specimens from 59 patients undergoing oral-maxillofacial surgery were imaged in detail by using a benchtop swept-source OCT system. It is shown that different lesions or tissues can be obviously distinguished based on their different microstructural features in OCT images, and the features are similar to those of their corresponding histopathological images. It is proven that OCT has great feasibility and potential as a diagnostic aid for surgeons in oral medicine.

Keywords: Oral-maxillofacial lesions; optical coherence tomography; intraoperative imaging; feasibility assessment.

¶Corresponding author.

---

1. Introduction

Oral cancer ranks eighth among the most common cancers in the world, and the five-year survival rate of patients is still less than 60%.[1] Surgery is one of the most common and effective methods to treat oral cancer. During surgeries, fast assessment of excised tissues can help surgeons to make intraoperative decisions. Nowadays, histopathological examination is still the gold standard for oral lesions, but it is time-consuming and can hardly be performed in real time. Visual examination is the most commonly used method for diagnosing oral and oral-maxillofacial lesions, but the accuracy is highly dependent on the experience of the surgeons. Intraoperative frozen section plays an important role in decision on the nature of lesions and selection of schema of operation, but it needs about 30 min to obtain pathological diagnosis.

Resolutions of ultrasound imaging, X-ray computed tomography and magnetic resonance imaging are not enough to accurately identify oral lesions in most cases. The characteristics such as high resolution and noninvasiveness make optical imaging techniques have a great potential in biomedicine. Fluorescence imaging,[2–4] two- and multi-photon microscopies,[5,6] confocal microscopy[7,8] and higher harmonic generation microscopy[9,10] have been studied in recent years. Fluorescence imaging often needs appropriate fluorescent agents and their safety needs to be carefully verified. In contrast, as a noninvasive method, optical coherence tomography (OCT) has the advantages of real-time, *in-vivo* and larger-depth imaging. OCT has developed rapidly since its introduction in 1991 (Ref. 11) and has been successfully applied in ophthalmology, cardiology and gastroenterology as a sophisticated diagnostic technique.

In oral medicine, many researches have been proposed to image oral diseases by OCT. Matheny *et al.* used OCT to image hamster cheek pouches with induced dysplasia and malignancies.[12] Wilder-Smith *et al.* introduced OCT to image hamster cheek pouches in order to observe the epithelial and subepithelial changes of oral carcinogenesis[13] and development of chemotherapy-induced mucositis.[14] Chen and co-workers showed the two-dimensional (2D) and three-dimensional (3D) OCT image volumes of normal and precancerous lesions of hamster cheek pouch specimens to evaluate the feasibility of OCT for the diagnosis of multiple stages of oral cancer progression.[15] They further constructed 3D OCT images and realized visualization of the extent and localization of tumor margins.[16] Ridgway *et al.* combined OCT with endoscopic photography for the identification of normal and abnormal microstructures in oral cavity and oropharynx.[17] Yang and co-workers used OCT to scan oral precancer and cancer, and analyze the characteristics of oral mucosa lesions in different oral carcinogenesis stages.[18–21] Jerjes *et al.* compared the OCT images and histopathological results of suspicious oral lesions to assess the feasibility of OCT in identifying malignant tissue.[22] Davoudi *et al.* used spectral-domain OCT (SD-OCT) to visualize the microstructural morphology and microvasculature in the human oral cavity and demonstrated the feasibility of microvascular imaging of healthy and pathological oral tissues.[23] Adegun *et al.* studied OCT to quantitatively differentiate normal and dysplastic oral epithelial samples.[24] Chen *et al.* proposed the combination of structural and vascular OCT imaging for the investigation of disease-related changes.[25] Wang and co-workers further reported the development of optical coherence tomography angiography to image blood flow within the microcirculatory tissue beds in human oral cavity *in vivo* with a wide field of view.[26]

Intraoperative imaging *ex vivo* can obtain imaging results closest to those of *in-vivo* imaging. In this study, a home-made swept-source OCT (SS-OCT) system with high speed and high sensitivity was used to scan and image hundreds of locations in 59 patients with more than 11 kinds of oral-maxillofacial lesions. It is demonstrated that the features of the OCT images are nearly the same as those of their corresponding histopathological images, and proved OCT had great potential in oral medicine to distinguish normal tissues (NTs), benign and malignant oral-maxillofacial tissues, and further proved the feasibility and potential of OCT as a diagnostic aid for surgeons in oral medicine. To the best of our knowledge, this is the first study discussing the OCT intraoperative imaging of various types of oral-maxillofacial lesions in detail.

2. Materials and Methods

2.1. *Materials*

Fresh excised human oral-maxillofacial tissue specimens from 59 patients undergoing oral lesionectomy at the Tianjin Stomatological Hospital,

Table 1. The information of lesions.

No.	Lesion	Cases	Type
1	Adenoid cystic carcinoma	2	Malignant
2	Squamous cell carcinoma	14	Malignant
3	Basal cell carcinoma	1	Malignant
4	Lipoma	1	Benign
5	Fibrous epulis	3	Benign
6	Ameloblastoma	1	Benign
7	Pleomorphic adenoma	9	Benign
8	Cyst tissue	8	Benign
9	Leukoplakia	6	Benign
10	Warthin tumor	3	Benign
11	Inflammatory tissue	11	Inflammatory

Tianjin, China were scanned by our home-made benchtop OCT system. The protocol was approved by the Ethics Committee of Tianjin Stomatological Hospital.

The patients' ages range from 20 years to 73 years. About 53% of them are male and 47% are female. The surgical sites included jaw, cheek, palate, tongue, neck, gingiva, parotid gland, etc. The information of lesions is shown in Table 1.

2.2. *OCT system*

Details of our home-made benchtop SS-OCT system were described in our previous paper.[27] As shown in Fig. 1, the swept source with 1310-nm center wavelength has 87-nm tunable range, 100-kHz swept rate and 20-mW output power. A 90/10 fiber coupler was used to split the beam between the sample and reference arms. The axial and transverse resolutions of the system are 14 μm (in air) and 17 μm, respectively. Interference signal was detected by a balanced photodetector.

2.3. *Experimental design*

Tissues were placed in a sterile dish and imaged by the OCT system to obtain the 2D and 3D OCT images immediately after surgery resection, and then they were fixed in formalin solution, embedded, sliced and stained. Finally, histology slides were viewed independently by a specialized pathologist at the Tianjin Stomatological Hospital to assess whether the slice contained malignant or normal tissue, and the final pathology report was generated. Histology slides from the OCT imaging areas were digitized with a microscope and matching camera, and comparisons were made with OCT images of the corresponding histologic sections.

During intraoperative imaging, it is not allowed to identify OCT-imaged area by the application of surgical ink. OCT imaging is performed in planes orthogonal to the histologic sectioning planes. Therefore, in order to obtain the best match, we tried to keep both directions of OCT scanning and the incision of the tissue by the pathologist the same as the direction of incision in the operating room in our study. Finally, a suitable section of 3D OCT images to match histopathological slides in the OCT imaged areas was found.

3. Experimental Results

OCT images with a field of view $6 \times 6\,\text{mm}^2$ from more than hundreds of locations for 59 patients were obtained. Representative OCT and histopathological images are shown in Figs. 2–12, respectively. Scale bars in all images are 1 mm.

Examples of OCT images of adenoid cystic carcinoma (ACC) are shown in Fig. 2. Figures 2(a) and 2(c) are the photos of palate tissues of two

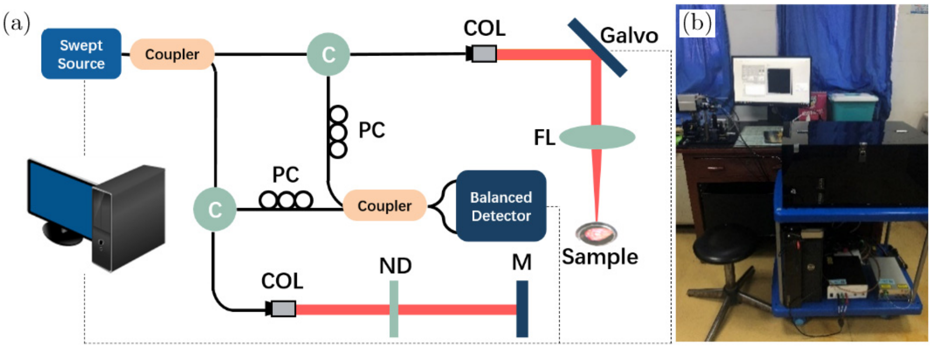

Fig. 1. (a) Schematic graph of the benchtop SS-OCT system. (b) Photo of the system during experiments in hospital. C: circulator, COL: collimating lens, PC: polarization controller, ND: neutral density filter, FL: focusing lens and M: mirror.

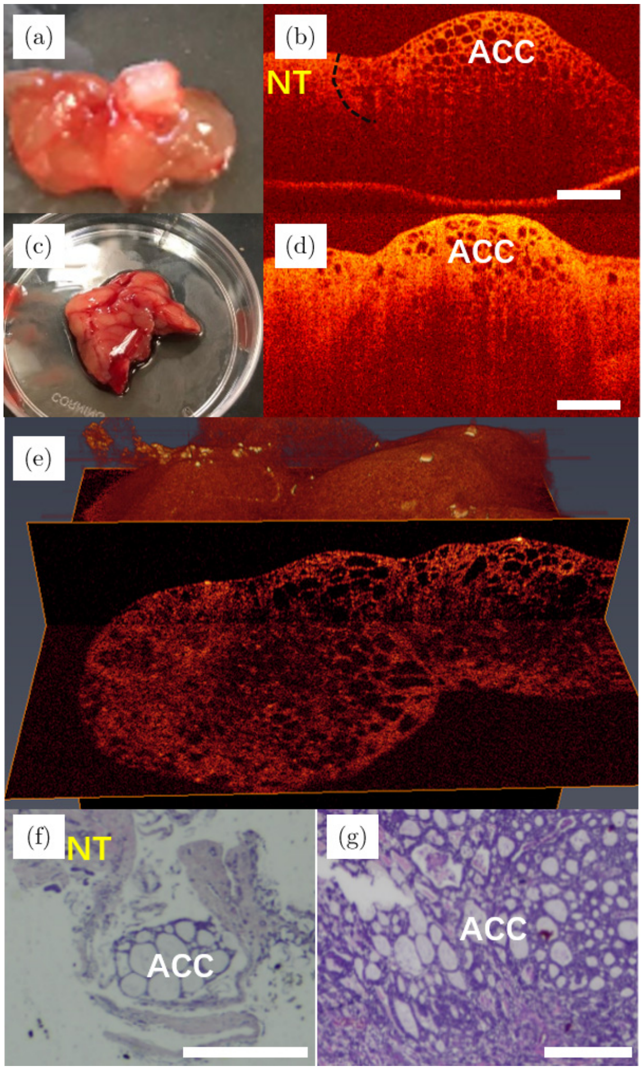

Fig. 2. Images of adenoid cystic carcinoma. Panels (a) and (c) are photos, and panels (b) and (d) are the 2D OCT images of adenoid cystic carcinoma of the palate tissue from two patients, respectively. Panel (e) is the 3D OCT image of the adenoid cystic carcinoma. Panels (f) and (g) are their corresponding histopathological images. ACC: adenoid cystic carcinoma and NT: normal tissue.

patients. Figures 2(b) and 2(d) show the 2D OCT images of the mixed cancerous tissues and NTs. As shown in Fig. 2(b), the black dotted curve indicates the boundary of ACC and NT. On the right-hand side of the black dotted curve is the area destroyed by cancerous tissues, and the region is not invaded on the left-hand side. From Fig. 2(b), it can be seen that the noncancerous areas show homogeneous scattering, whereas tightly arranged round bubbles with different sizes and irregular shapes have emerged in the cancerous tissue. Irregular cribriform structures are typical features of adenoid cystic carcinoma. Figure 2(e) is the 3D OCT image of the palate tissues. Cancerous tissue of cribriform structures can be seen from different perspectives. Their corresponding histopathological images are shown in Figs. 2(f) and 2(g).

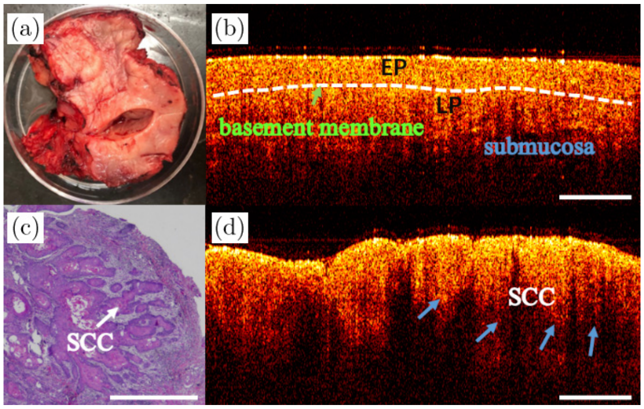

Fig. 3. OCT and the corresponding histology of SCC. (a) Photo of the excised tissue specimen. (b) and (d) The 2D OCT images of two different positions from the same specimen. Panel (b) shows normal oral mucosa, and panel (d) shows the SCC. (c) The corresponding histopathological image of SCC. SCC: squamous cell carcinoma, EP: epithelial layer and LP: lamina propria.

Typical examples of OCT images of squamous cell carcinoma (SCC) are shown in Fig. 3. The photo of the tongue with SCC is shown in Fig. 3(a). The epithelial layer (denoted as EP in the figure) and the lamina propria (LP) are clearly visible for normal oral mucosa. As shown in the OCT image from normal mucosa [Fig. 3(b)], the boundary between epithelial layer and LP is indicated by the white dashed line. Unlike normal mucosa, SCC is epithelial invasive carcinoma with varying degrees of squamous differentiation, and consists of irregular squamous epithelium of nest- or cord-like hyperplasia. The corresponding histopathological image is shown in Fig. 3(c). As shown in Fig. 3(d), the boundary of epithelial layer and LP is unclear, and the basement membrane (BM) is destroyed. As indicated by the blue arrows, squamous cell carcinoma is shown as the cord-like structures.

Images of basal cell carcinoma (BCC) are shown in Fig. 4. Figure 4(a) shows the photo of excised BCC. BCC is a malignant tumor characterized by basaloid cells with a cylinder-, ribbon- or cord-like hyperplasia. It belongs to a kind of local invasive tumor. As shown in Figs. 4(b) and 4(d), the epithelial tissue (denoted as EP in the figure) exhibits a high density that has stronger scattering than that

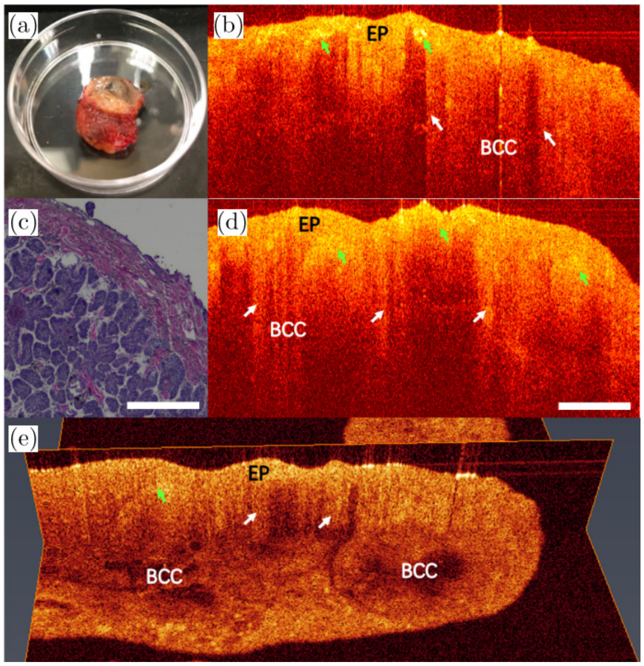

Fig. 4. Images of the BCC. Photo [panel (a)] and 2D OCT images [panels (b) and (d)] of BCC removed from a patient, along with the corresponding histopathological image [panel (c)]. (e) The 3D OCT image. EP: epithelial tissue and BCC: basal cell carcinoma.

of LP. The basement membrane is destroyed due to basal-like cell infiltration, as indicated by the white arrows. The areas represented by green arrows show higher tissue density, inhomogeneous scattering and deformation of the tissue structures on account of cell proliferation. Therefore, there are cord-like shadow areas below the epithelial layer in their OCT images. The corresponding histopathological image is shown in Fig. 4(c). Figure 4(e) shows its 3D OCT image. The basaloid cell infiltration can be clearly viewed.

Images of lipoma are shown in Fig. 5. Figure 5(a) is the photo of the excised specimen. The scanning position is shown by a black line in Fig. 5(a). A typical OCT image of lipoma [Fig. 5(b)] shows its inhomogeneous scattering. Fibrous tissues (FTs) that do not contain fat granules are arranged closely, and they are homogeneous structures and the regions of higher tissue density have stronger scattering than those of the background and fat tissues in the OCT image, as indicated by black arrows in Fig. 5(b). However, as indicated by white arrows in Fig. 5(b), fat vesicles (FVs) malignantly occupy fibrous tissue regions, leading to tissue stratification and heterogeneity. The reticular fibrous tissue envelops the clusters of fat cells, forming loose microporous structures in the OCT image. The corresponding histology image is shown in Fig. 5(c). The black arrows and white arrows indicate fibrous tissues and fat tissues, respectively.

Images of fibrous epulis (FE) are shown in Fig. 6. Figure 6(a) is the photo of the excised tissue specimen. Figures 6(b) and 6(c) are the 2D and 3D OCT images, respectively. According to pathology, FE is mainly caused by hyperplasia of fibrous tissue under the gingival epithelium. The green arrows in Fig. 6(b) indicate the boundary of epithelium (denoted as EP in the figure) and fibrous tissues. Epithelial tissue is more homogeneous than fibrous tissues and has higher scattering. The 3D OCT image [Fig. 6(c)] exhibits clear boundaries of epithelium and fibrous connective tissues from different directions, as well as the underlying hyperplasticized fibrous tissue structure, as indicated by the green arrows. The corresponding pathology image is shown in Fig. 6(d). The tissue boundary is shown by green arrows. There are little holes in the epithelium in the pathological image. Correspondingly, from the *en-face* OCT image of epithelial layer pointed out by a black dashed line in Fig. 6(b), some little holes can be seen clearly. These holes are the cross-section of epithelium rete, which are filled with connective tissue papillae.

Figure 7 shows the photo of the excised specimen, 2D and 3D OCT images and the corresponding

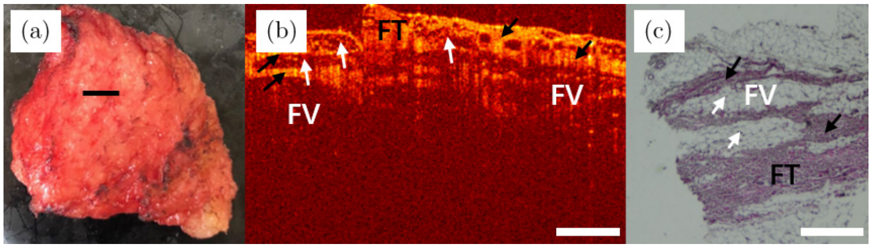

Fig. 5. Images of lipoma. (a) Photo of the excised tissue specimen. (b) An OCT image of lipoma. (c) Its corresponding histopathological image. FT: fibrous tissue and FV: fat vesicle.

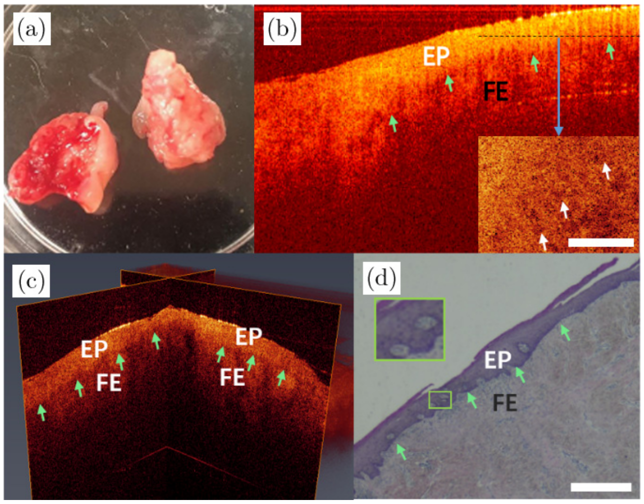

Fig. 6. Images of fibrous epulis. (a) Photo of the excised tissue specimen. (b) The 2D OCT image and *en-face* OCT image from the dashed line of fibrous epulis. (c) The 3D OCT image and (d) its histopathological image. EP: epithelial tissue and FE: fibrous epulis.

histology of the mandibular from a patient with ameloblastoma. The center of the scanning position is shown by the black line in Fig. 7(a). The OCT image in Fig. 7(b) shows a heterogeneous tissue structure with chaotic distribution of high-density scattering regions and low-density scattering regions, similar to plaques. That is a typical manifestation of ameloblastoma, called follicular pattern. As shown by the white arrows in Fig. 7(b), the tumor forms some isolated epithelial islands. Follicular ameloblastoma (FA) usually develops cystic changes in the center of the follicles. Figure 7(d) shows the ameloblastoma with cystic changes compared to Fig. 7(b), as indicated by the white arrows. The cystic structure of follicular ameloblastoma (CFA) is correspondingly shown in its histopathological image of Fig. 7(c). The red arrow indicates the tumor tissue and the black arrow is the connective tissue. As shown by the black arrow in black box, the stroma between follicles is a loose connective tissue, which is shown as pink after hematoxylin–eosin staining (H&E). The 3D reconstructed OCT image is shown in Fig. 7(e). In different directions, the 3D OCT image shows different lesion areas, as indicated by the white ovals.

The photo of excised pleomorphic adenoma (PA) of submandibular gland is shown in Fig. 8(a). OCT images of two different scanning positions are shown in Figs. 8(b) and 8(d), respectively. The morphological features of PAs are diverse, one of which is typically a cell-rich solid region arranged in clusters, as indicated in its histopathological image [Fig. 8(c)]. The OCT image in Fig. 8(b) shows the boundary of fibrous capsule (FC), as indicated by the blue arrows. The aligned fibrous tissues in capsule form bright bands, as shown by the white arrows, whereas the region under fibrous capsule shows irregular shadows due to the clumps of tumor tissues. Figure 8(d) is the OCT image of another area scanned from the same sample, in which white arrows represent the bright band of the fibrous tissues in the FC imaged by the OCT system as indicated in Fig. 8(b). As shown in Fig. 8(e), the pleomorphic adenoma morphology can be clearly seen in its 3D OCT image, where the fibrous capsule can be more directly perceived. The white arrows show bright bands in the fibrous capsule.

Figure 9 is the image of sublingual gland. Figure 9(a) is the photo of the sublingual gland removed from a patient with sublingual cyst (C), and the OCT images of the specimen are shown in Figs. 9(b) and 9(d). The sublingual gland is mainly composed of mucinous acinus and multiple acinar cells forming glandular lobules (GLs), which are separated by fibrous connective tissues (FCTs). Its *en-face* OCT image is shown in Fig. 9(c). Glandular lobules composed of acinus are less scattering than fibrous connective tissue, so the areas of GL are clearly distinguishable from the *en-face* image. The corresponding histology image is shown in Fig. 9(e). White arrows represent the fibrous connective tissues, and black arrows represent the glandular lobules in Fig. 9. Figure 9(f) is the 3D reconstructed OCT image, where boundaries are clearly seen from different perspectives.

Photographs, OCT and histopathological images of leukoplakia from three patients are shown in Fig. 10. According to the view of oral histopathology, verrucous leukoplakia [Fig. 10(a)] belongs to nonhomogeneous leukoplakia with irregular surface, verrucous, nodular, papillary and hyperkeratotic epithelium, as indicated by the white arrows in Fig. 10(b), where many papillae can be seen on the epithelium in its OCT image. Whereas, the surface of homogeneous leukoplakia [Fig. 10(d)] is relatively flat, as shown by the black arrows in Fig. 10(e). The epithelium is mainly composed of keratinocytes, and its OCT image shows stronger scattering relative to LP. The epithelium in Fig. 10(e) is thickened, as indicated by the black double arrow. For verrucous leukoplakia and homogeneous leukoplakia, the

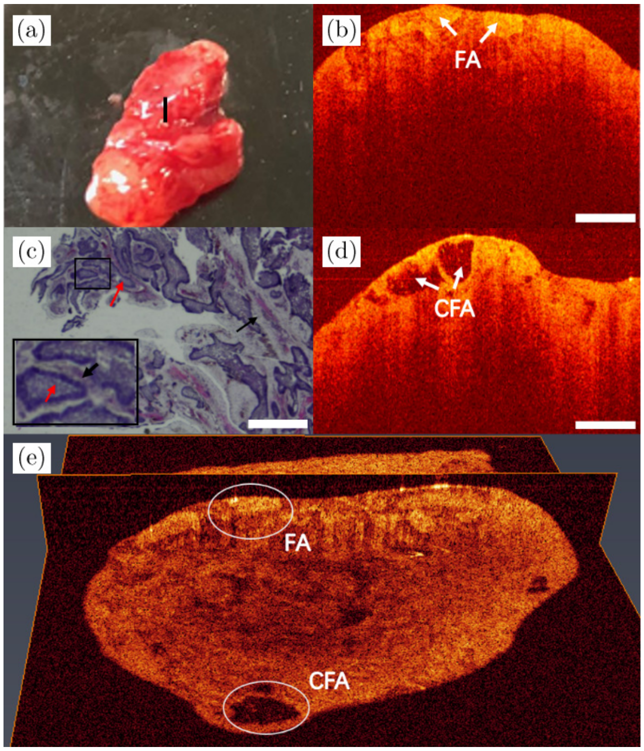

Fig. 7. Images of ameloblastoma. (a) Photo of the excised tissue specimen. (b) and (d) Two 2D OCT images from different positions with follicular ameloblastoma. (c) Its histopathological image. (e) A 3D OCT image, the white ovals indicate the lesion areas. FA: follicular ameloblastoma and CFA: cystic structure of follicular ameloblastoma.

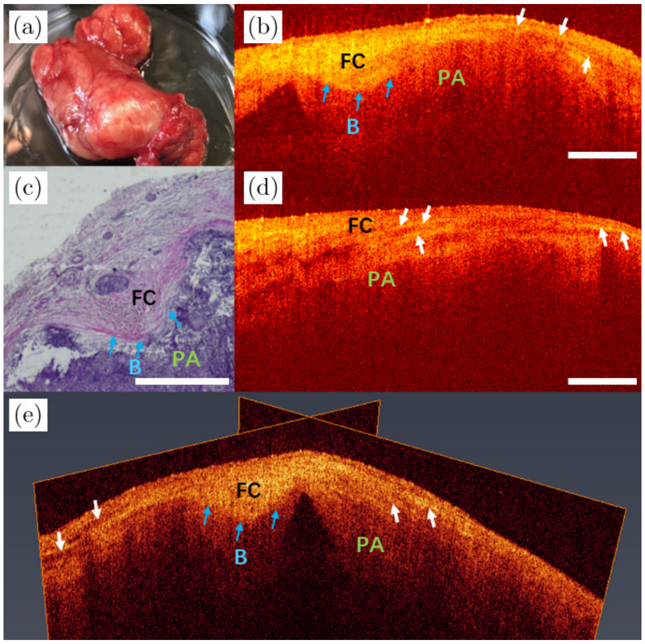

Fig. 8. Images of pleomorphic adenoma of submandibular gland. (a) The photo of the excised tissue. (b) and (d) Two 2D OCT images of different positions of pleomorphic adenomas from the same sample. (c) Its histopathological image. (e) A 3D OCT image. PA: pleomorphic adenoma, FC: fibrous capsule and B: boundary.

basement membranes are clear, as indicated by the white dash-dotted curve in Figs. 10(b) and 10(e), respectively. For leukoplakia canceration [Fig. 10(g)], its epithelial surface is incompletely keratinized. Epithelial cells are abnormally proliferated, and have partially infiltrated into the connective tissues, as indicated by the green arrows in Fig. 10(h). The OCT image of early invasive carcinoma showed uniform scattering due to severe dysplasia of epithelium, so the basement membranes cannot be clearly identified. The corresponding histopathological images are shown in Figs. 10(c), 10(f) and 10(i), respectively.

An example of OCT image of papillary cystadenoma lymphomatosum/Warthin tumor (WT) is shown in Fig. 11. WT is composed of adenoid structures, often cystic structures, sometimes papillary structures. This kind of tumor often occurs in the parotid gland. In pathology, WT often has cracks and cysts of different sizes, and the contents of the capsule can be transparent, yellowish, mucoid, milky white liquid, etc. Under optical microscopy, WT consists of double epithelium and lymphocytes. Figure 11(a) is the WT of the parotid gland, where the position of the OCT scanning is shown by a black line. The OCT image of WT in

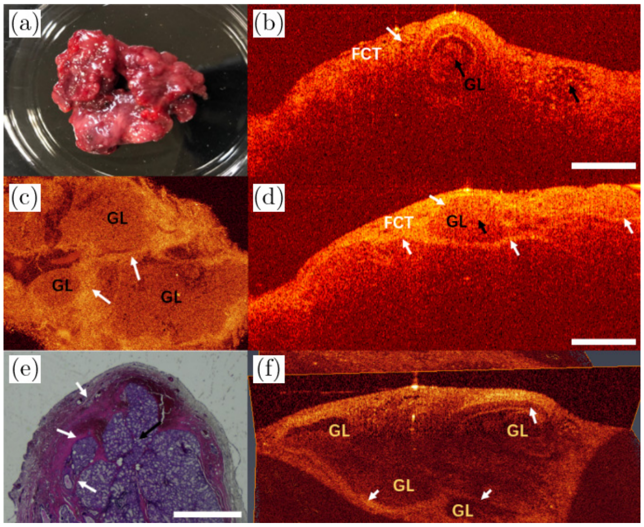

Fig. 9. Images of sublingual gland. (a) Photo of the excised tissue specimen. (b) and (d) The 2D OCT images of two different positions of sublingual gland from the same sample. (c) An *en-face* image. (e) Its histopathological image. (f) A 3D OCT image. FCT: fibrous connective tissue and GL: glandular lobule.

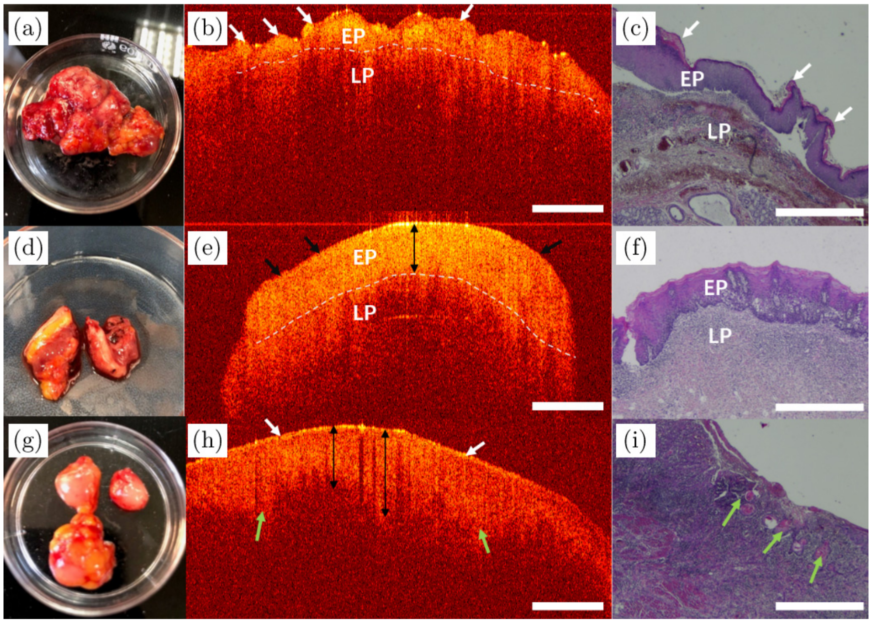

Fig. 10. OCT images and their histopathological images of leukoplakia. Panels (a) and (d) are photos, and panels (b) and (e) are the 2D OCT images of leukoplakia from two patients, respectively. Panel (g) is the photo and panel (h) is the 2D OCT image of leukoplakia canceration. Panels (c), (f) and (i) are the corresponding histopathological images of panels (a), (d) and (g), respectively. EP: epithelial layer and LP: lamina propria.

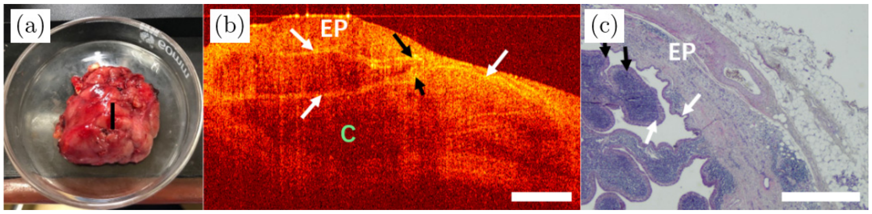

Fig. 11. Images of WT. (a) Photo of the excised tissue specimen. (b) The 2D OCT image of WT. (c) Its histopathological image. EP: epithelial tissue, WT: Warthin tumor and C: cyst.

Fig. 11(b) shows the cyst structure and double-layer epithelium, as indicated by the white arrows. The corresponding histopathological image is shown in Fig. 11(c). The papillary structures can be seen as indicated by the black arrows in Figs. 11(b) and 11(c).

Images of submandibular gland inflammation are shown in Fig. 12. Chronic sclerosing submandibular gland inflammation is characterized by inflammatory infiltration around the glandular lobes, especially around the ducts and acinus, and infiltrating lymphocytes aggregate to form irregular lymphoid

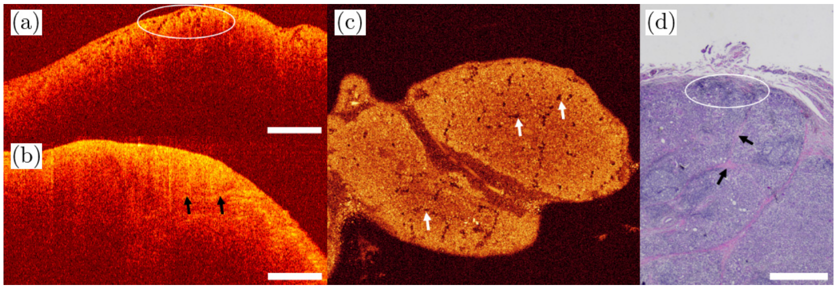

Fig. 12. Images of submandibular gland tissue. Cross-sectional OCT images [panels (a) and (b)] and its *en-face* OCT image [panel (c)] showing submandibular gland inflammation. (d) The corresponding histopathological image.

follicles. Moreover, the interstitial of the gland has obvious fibrosis, and the acinar atrophy due to inflammatory infiltration. As indicated in the elliptical curve in Fig. 12(a), small follicles with lower scattering exist in the OCT image. Figure 12(b) exhibits significant fibrosis of the interstitial, where connective tissues are markedly thickened as indicated by the black arrows. Its *en-face* OCT image is shown in Fig. 12(c). White arrows indicate clearly inflammatory cell aggregation and acinar atrophy. The corresponding histopathological image is shown in Fig. 12(d).

4. Discussions and Conclusion

Taking the fresh excised oral-maxillofacial tissues from 59 patients as examples, different oral-maxillofacial lesions expressed discriminable structure features in OCT images, and have the nearly same characteristics as their corresponding histopathological images, which demonstrated the great potential of translation of OCT imaging from the bench to the operating room and it can help surgeons diagnose lesions rapidly.

In order to apply OCT to oral clinical applications including biopsy guidance and routine screening, we think the appropriate design of oral probes is the critical factor for applying OCT to the complex oral environment. For *in-vivo* clinical imaging, some areas, such as the buccal mucosa and upper jaw, are difficult to be detected. We have finished a forward-viewing compact probe based on a dual-axis MEMS scanner, whose rigid part is 70 mm in length and 7 mm in diameter. It exhibits excellent flexibility and can obtain similar results to those of the scanning galvanometer with an axial resolution of $\sim 12\,\mu$m (in tissue) and a lateral resolution of $\sim 9\,\mu$m. The design of the probe is still being improved in order to be applied in clinic finally.

In addition, we think the following further study need to be done. First, it must be fully proven that it has the ability to distinguish different diseases based on its collected images. More patients and more types of lesions *ex vivo* and *in vivo* should be scanned and comparison data should be further accumulated. Second, imaging quality and system performance are important for clinic translation, OCT system with higher axial and lateral resolutions will be better for the identification of oral-maxillofacial tissue lesions. Third, simplifying the OCT data collection process will also make the software operation more time-saving, and what is more, although lesions can be detected based on the structure information of tissues in OCT images, quantitative analysis of OCT images like in Refs. 22–24 is more desirable.

Conflict of Interest

All of the authors have no relevant financial interests in this paper and no potential conflicts of interest to disclose.

Acknowledgments

This work was supported by National Natural Science Foundation of China (NSFC) (61875092 and 11374167), State Key Project of Research and Development Plan (2016YFC0101002), Science and Technology Support Program of Tianjin (17YFZCSY00740) and Fundamental Research Funds for the Central Universities of Nankai University (63191203).

References

1. R. L. Siegel, K. D. Miller, A. Jemal, “Cancer statistics, 2019,” *CA Cancer J. Clin.* **69**(1), 7–34 (2019).
2. N. Kanchwala, N. Kumar, S. Gupta, H. Lokhandwala, “Fluorescence spectroscopic study on malignant and premalignant oral mucosa of patients undergoing treatment: An observational prospective study,” *Int. J. Surg.* **55**, 87–91 (2018).
3. P. A. Pellionisz, K. W. Badran, W. S. Grundfest, M. A. St. John, “Detection of surgical margins in oral cavity cancer: The role of dynamic optical contrast imaging,” *Curr. Opin. Otolaryngol. Head Neck Surg.* **26**(2), 102–107 (2018).
4. L. E. Simonato, S. Tomo, G. I. Miyahara, R. S. Navarro, A. G. J. B. Villaverde, “Fluorescence visualization efficacy for detecting oral lesions more prone to be dysplastic and potentially malignant disorders: A pilot study,” *Photodiagnosis Photodyn. Ther.* **17**, 1–4 (2017).
5. H. Guo, H.-W. Wang, Q. Tang, E. Anderson, R. Falola, T. Smith, Y. Liu, M. Levi, P. M. Andrews, Y. Chen, “Intravital imaging of adriamycin-induced renal pathology using two-photon microscopy and optical coherence tomography,” *J. Innov. Opt. Health Sci.* **11**(5), 1850030 (2018).

6. A. G. Ammer, K. E. Hayes, K. H. Martin, L. Zhang, G. A. Spirou, S. A. Weed, "Multi-photon imaging of tumor cell invasion in an orthotopic mouse model of oral squamous cell carcinoma," *J. Vis. Exp.* **53**, e2941 (2011).
7. R. Samatham, K. G. Phillips, S. L. Jacques, "Assessment of optical clearing agent using reflectance-mode confocal scanning laser microscopy," *J. Innov. Opt. Health Sci.* **3**(3), 183–188 (2010).
8. J. M. Jabbour, J. L. Bentley, B. H. Malik, J. Nemechek, J. Warda, R. Cuenca, S. Cheng, J. A. Jo, K. C. Maitland, "Reflectance confocal endomicroscope with optical axial scanning for *in vivo* imaging of the oral mucosa," *Biomed. Opt. Express* **5**(11), 3781–3791 (2014).
9. S.-P. Tai, W.-J. Lee, D.-B. Shieh, P.-C. Wu, H.-Y. Huang, C.-H. Yu, C.-K. Sun, "*In vivo* optical biopsy of hamster oral cavity with epi-third-harmonic-generation microscopy," *Opt. Express* **14**(13), 6178–6187 (2006).
10. M.-R. Tsai, D.-B. Shieh, P.-J. Lou, C.-F. Lin, C.-K. Sun, "Characterization of oral squamous cell carcinoma based on higher-harmonic generation microscopy," *J. Biophotonics* **5**(5–6), 415–424 (2012).
11. D. Huang, E. A. Swanson, C. P. Lin, J. S. Schuman, W. G. Stinson, W. Chang, M. R. Hee, T. Flotte, K. Gregory, C. A. Puliafito, J. G. Fujimoto, "Optical coherence tomography," *Science* **254**(5035), 1178–1181 (1991).
12. E. S. Matheny, N. M. Hanna, W. G. Jung, Z. Chen, P. Wilder-Smith, R. Mina-Araghi, M. Brenner, "Optical coherence tomography of malignancy in hamster cheek pouches," *J. Biomed. Opt.* **9**(5), 978–981 (2004).
13. P. Wilder-Smith, W.-G. Jung, M. Brenner, K. Osann, H. Beydoun, D. Messadi, Z. Chen, "*In vivo* optical coherence tomography for the diagnosis of oral malignancy," *Lasers Surg. Med.* **35**(4), 269–275 (2004).
14. P. Wilder-Smith, M. J. Hammer-Wilson, J. Zhang, Q. Wang, K. Osann, Z. Chen, H. Wigdor, J. Schwartz, J. Epstein, "*In vivo* imaging of oral mucositis in an animal model using optical coherence tomography and optical Doppler tomography," *Clin. Cancer Res.* **13**(8), 2449–2454 (2007).
15. W. Jung, J. Zhang, J. Chung, P. Wilder-Smith, M. Brenner, J. S. Nelson, Z. Chen, "Advances in oral cancer detection using optical coherence tomography," *IEEE J. Sel. Top. Quantum Electron.* **11**(4), 811–817 (2005).
16. N. M. Hanna, W. Waite, K. Taylor, W.-G. Jung, D. Mukai, E. Matheny, K. Kreuter, P. Wilder-Smith, M. Brenner, Z. Chen, "Feasibility of three-dimensional optical coherence tomography and optical Doppler tomography of malignancy in hamster cheek pouches," *Photomed. Laser Surg.* **24**(3), 402–409 (2006).
17. J. M. Ridgway, W. B. Armstrong, S. Guo, U. Mahmood, J. Su, R. P. Jackson, T. Shibuya, R. L. Crumley, M. Gu, Z. Chen, B. J.-F. Wong, "*In vivo* optical coherence tomography of the human oral cavity and oropharynx," *Arch. Otolaryngol. Head Neck Surg.* **132**(10), 1074–1081 (2006).
18. M.-T. Tsai, H.-C. Lee, C.-K. Lee, C.-H. Yu, H.-M. Chen, C.-P. Chiang, C.-C. Chang, Y.-M. Wang, C. C. Yang, "Effective indicators for diagnosis of oral cancer using optical coherence tomography," *Opt. Express* **16**(20), 15847–15864 (2008).
19. M.-T. Tsai, H.-C. Lee, C.-W. Lu, Y.-M. Wang, C.-K. Lee, C.-C. Yang, C.-P. Chiang, "Delineation of an oral cancer lesion with swept-source optical coherence tomography," *J. Biomed. Opt.* **13**(4), 044012 (2008).
20. M.-T. Tsai, C.-K. Lee, H.-C. Lee, H.-M. Chen, C.-P. Chiang, Y.-M. Wang, C.-C. Yang, "Differentiating oral lesions in different carcinogenesis stages with optical coherence tomography," *J. Biomed. Opt.* **14**(4), 044028 (2009).
21. C.-K. Lee, T.-T. Chi, C.-T. Wu, M.-T. Tsai, C.-P. Chiang, C.-C. Yang, "Diagnosis of oral precancer with optical coherence tomography," *Biomed. Opt. Express* **3**(7), 1632–1646 (2012).
22. W. Jerjes, T. Upile, B. Conn, Z. Hamdoon, C. S. Betz, G. McKenzie, H. Radhi, M. Vourvachis, M. E. Maaytah, A. Sandison, A. Jay, C. Hopper, "*In vitro* examination of suspicious oral lesions using optical coherence tomography," *Br. J. Oral Maxillofac. Surg.* **48**(1), 18–25 (2010).
23. B. Davoudi, A. Lindenmaier, B. A. Standish, G. Allo, K. Bizheva, A. Vitkin, "Noninvasive *in vivo* structural and vascular imaging of human oral tissues with spectral domain optical coherence tomography," *Biomed. Opt. Express* **3**(5), 826–839 (2012).
24. O. K. Adegun, P. H. Tomlins, E. Hagi-Pavli, G. McKenzie, K. Piper, D. L. Bader, F. Fortune, "Quantitative analysis of optical coherence tomography and histopathology images of normal and dysplastic oral mucosal tissues," *Lasers Med. Sci.* **27**(4), 795–804 (2012).
25. P.-H. Chen, C.-H. Wu, Y.-F. Chen, Y.-C. Yeh, B.-H. Lin, K.-W. Chang, P.-Y. Lai, M.-C. Hou, C.-L. Lu, W.-C. Kuo, "Combination of structural and vascular optical coherence tomography for differentiating oral lesions of mice in different carcinogenesis stages," *Biomed. Opt. Express* **9**(4), 1461–1476 (2018).

26. W. Wei, W. J. Choi, R. K. Wang, "Microvascular imaging and monitoring of human oral cavity lesions *in vivo* by swept-source OCT-based angiography," *Lasers Med. Sci.* **33**(1), 123–134 (2018).

27. F. Hou, M. Zhang, Y. Zheng, L. Ding, X. Tang, Y. Liang, "Detection of laser-induced bulk damage in optical crystals by swept-source optical coherence tomography," *Opt. Express* **27**(3), 3698–3709 (2019).